An asymptotic factorization method for inverse electromagnetic scattering in layered media II: A numerical study

Roland Griesmaier and Martin Hanke

Abstract. We investigate the performance of a MUSIC-type algorithm for low frequent time-harmonic electromagnetic imaging of the subsurface. This algorithm is based on an asymptotic analysis and an associated asymptotic factorization of electromagnetic near field data in the presence of very small scatterers in the ground. Our numerical results illustrate the potential of this imaging method, and we provide theoretical evidence for what has been observed numerically. In particular, we address the issue of superresolution which, in this context, means that it is possible to use this method to reconstruct objects of centimeters in size, and separated by only few multiples of their diameters, despite the fact that the given time-harmonic electromagnetic waves may have wavelengths that are several kilometers long.

1. Introduction

Since the seminal paper by Devaney [13] there has been an increasing interest in imaging techniques for inverse obstacle problems along the lines of the celebrated MUSIC algorithm. We refer to Cheney [8] for a brief survey of this algorithm and its relation to inverse problems and imaging. A rigorous foundation of these MUSIC-type methods can be given along the lines developed in [7], which amounts to an asymptotic analysis of the given input data for the corresponding inverse problem, as the size of the obstacles converges to zero. Typically, these measurements can be interpreted in the limit as the data corresponding to an inverse source problem, with the infinitesimal obstacles acting as (fictitious) point sources. A good survey about the corresponding state of the art can be found in the books by Ammari and Kang [2, 3].

In the present paper we address a particular instance of these methods related to low-frequent subsurface electromagnetic imaging, intended to combine off-the-shelf metal detectors for taking multistatic data for time-harmonic electromagnetic induction tomography of the soil. This problem had originially been raised and funded by the German Federal Ministery of Education and Research (BMBF) to improve the performance of commercial metal detectors for humanitarian demining, cf. [18].

2000 *Mathematics Subject Classification.* Primary 78A46, 35R30, 35Q60, 35C20.

While the asymptotic analysis from [16, 17] provides all relevant information about the multistatic response data matrix that occurs in this context, the adaptation of the MUSIC idea to utilize this information is the major focus of this present work; we mention, though, that the imaging aspect has already been addressed in [17] briefly, but a considerable amount of insight gained in [16] is still waiting to be published.

During the preparation of the thesis [16], Iakovleva and Lesselier with varying coauthors [1, 19, 20] have utilized similar ideas for the same problem, essentially. Our findings nicely support and complement their results. In particular, we illuminate from various viewpoints the important issue of resolution limit that can be achieved with this imaging technique. We know of no other treatment of this topic of comparable depth.

The outline of our paper is as follows. In Section 2 we describe the basic modeling of our setting and summarize the results of the asymptotic analysis from [17]. The results are subsequently illustrated numerically in Section 3. In particular, we address some peculiarities that arise for the low frequencies that are typical for commercial metal detectors. For example, while the numerical rank of the limiting multistatic response matrix is a multiple of six in general, the low frequent fictitious electric sources in the scattering obstacles turn out to be almost negligible as compared to the corresponding magnetic sources. As a result the numerical (or essential) rank of the limiting matrix is a multiple of three, only, for low frequencies.

In Section 4 we turn to the inverse problem and describe the MUSIC-type algorithm that we are going to use to image the subsurface and the obstacles in there. We provide three numerical examples that illustrate the performance of this algorithm and indicate its ultimate limitations. As it turns out, the noise level, in combination with the ill-posedness of the problem, is the most important obstruction that needs to be dealt with. While this may not come as a surprise, we will go on and show in great detail in Secion 5 that, again, noise is also the only limitation in getting perfect resolution, far below the Nyquist barrier. We thus examplify that the method may be a worthwhile alternative for the electromagnetic imaging of small scatters in the ground.

2. The direct scattering problem for small scatterers

We start with a mathematical description of our setting. We fix $\Sigma_0 := \{\boldsymbol{x} \in \mathbb{R}^3 \mid x_3 = 0\}$ as the surface of ground, and decompose the entire space in the two halfspaces $\mathbb{R}^3_+$ and $\mathbb{R}^3_-$ above and below Σ_0 to correspond to air and ground, respectively. Both halfspaces are assumed to be filled with homogeneous materials. More precisely, the *electric permittivity* ε and the *magnetic permeability* μ are given by

$$\varepsilon(\boldsymbol{x}) := \begin{cases} \varepsilon_+, & \boldsymbol{x} \in \mathbb{R}^3_+, \\ \varepsilon_-, & \boldsymbol{x} \in \mathbb{R}^3_-, \end{cases} \qquad \mu(\boldsymbol{x}) := \begin{cases} \mu_+, & \boldsymbol{x} \in \mathbb{R}^3_+, \\ \mu_-, & \boldsymbol{x} \in \mathbb{R}^3_-, \end{cases}$$

where ε_+ as well as $\mu_\pm$ are positive numbers, whereas ε_- may be complex with positive real and nonnegative imaginary part to allow for conductive soils. By $\omega > 0$ we denote the angular velocity, and $k := \omega\sqrt{\varepsilon\mu}$ (with nonnegative imaginary part) is the associated (discontinuous) *wave number*.

We assume that electromagnetic fields are generated by *magnetic dipole distributions* with a dipole density $\boldsymbol{\varphi}$ on a two-dimensional device

$$\mathcal{M} \subset \Sigma_d := \{\boldsymbol{x} \in \mathbb{R}^3_+ \mid x_3 = d\}, \qquad d > 0,$$

in the upper halfspace. To be more specific, we introduce the *magnetic dyadic Green's function* $\mathbb{G}^m$ and the *electric dyadic Green's function* $\mathbb{G}^e$ as the (distributional) solutions of

$$\mathbf{curl}_x \frac{1}{\varepsilon(\boldsymbol{x})} \mathbf{curl}_x \mathbb{G}^m(\boldsymbol{x}, \boldsymbol{y}) - \omega^2 \mu(\boldsymbol{x}) \mathbb{G}^m(\boldsymbol{x}, \boldsymbol{y}) = \frac{1}{\varepsilon(\boldsymbol{x})} \delta(\boldsymbol{x} - \boldsymbol{y}) \mathbb{I}_3, \qquad \boldsymbol{x}, \boldsymbol{y} \in \mathbb{R}^3,$$

and

$$\mathbf{curl}_x \frac{1}{\mu(\boldsymbol{x})} \mathbf{curl}_x \mathbb{G}^e(\boldsymbol{x}, \boldsymbol{y}) - \omega^2 \varepsilon(\boldsymbol{x}) \mathbb{G}^e(\boldsymbol{x}, \boldsymbol{y}) = \frac{1}{\mu(\boldsymbol{x})} \delta(\boldsymbol{x} - \boldsymbol{y}) \mathbb{I}_3, \qquad \boldsymbol{x}, \boldsymbol{y} \in \mathbb{R}^3,$$

where $\mathbb{I}_3$ denotes the 3×3 identity matrix, together with the Silver-Müller radiation conditions

$$\int_{\partial B_R(0)} \Big| \frac{\boldsymbol{x}}{R} \times \mathbb{G}^{m/e}(\boldsymbol{x}, \boldsymbol{y}) + \frac{\mathrm{i}}{k(\boldsymbol{x})} \mathbf{curl}_x \mathbb{G}^{m/e}(\boldsymbol{x}, \boldsymbol{y}) \Big|^2 \, \mathrm{d}s(\boldsymbol{x}) = o(1) \qquad \text{as } R \to \infty,$$

$$\int_{\partial B_R(0)} \Big| \frac{\boldsymbol{x}}{R} \times \mathbf{curl}_x \mathbb{G}^{m/e}(\boldsymbol{x}, \boldsymbol{y}) + \mathrm{i}\, k(\boldsymbol{x}) \mathbb{G}^{m/e}(\boldsymbol{x}, \boldsymbol{y}) \Big|^2 \, \mathrm{d}s(\boldsymbol{x}) = o(1) \qquad \text{as } R \to \infty.$$

Then, for a magnetic dipole density $\boldsymbol{\varphi} \in L^2(\mathcal{M}; \mathbb{C}^3)$ the *incident field* $(\boldsymbol{E}^i, \boldsymbol{H}^i)$ is given by

$$\boldsymbol{H}^i := k_+^2 \int_{\mathcal{M}} \mathbb{G}^m(\cdot, \boldsymbol{y}) \boldsymbol{\varphi}(\boldsymbol{y}) \, \mathrm{d}s(\boldsymbol{y}), \quad \boldsymbol{E}^i := -\frac{1}{\mathrm{i}\,\omega\varepsilon} \mathbf{curl} \boldsymbol{H}^i \qquad \text{in } \mathbb{R}^3 \setminus \mathcal{M}. \tag{2.1}$$

Note that $(\boldsymbol{E}^i, \boldsymbol{H}^i)$ is a *radiating solution* of the time-harmonic *Maxwell equations*

$$\mathbf{curl} \boldsymbol{H}^i + \mathrm{i}\,\omega\varepsilon \boldsymbol{E}^i = 0, \quad \mathbf{curl} \boldsymbol{E}^i - \mathrm{i}\,\omega\mu \boldsymbol{H}^i = 0 \tag{2.2}$$

in $\mathbb{R}^3 \setminus \mathcal{M}$. By this we mean that $\boldsymbol{E}^i, \boldsymbol{H}^i \in \boldsymbol{H}_{\mathrm{loc}}(\mathbf{curl}, \mathbb{R}^3 \setminus \mathcal{M})$ is a weak solution of (2.2) which fulfills the integral radiation condition

$$\int_{\partial B_R(0)} \Big| \frac{\boldsymbol{x}}{R} \times \boldsymbol{H}^i(\boldsymbol{x}) + \Big(\frac{\varepsilon(\boldsymbol{x})}{\mu(\boldsymbol{x})} \Big)^{1/2} \boldsymbol{E}^i(\boldsymbol{x}) \Big|^2 \, \mathrm{d}s(\boldsymbol{x}) = o(1) \qquad \text{as } R \to \infty,$$

cf., e.g., Cutzach and Hazard [10], or Monk [23].

Next, we assume that $\mathbb{R}^3_-$ contains a finite collection of well separated small perfectly conducting scatterers, each of the form $D_{\delta,l} := \boldsymbol{z}_l + \delta B_l$, $1 \le l \le m$, where $B_l \subset \mathbb{R}^3$ is a smooth bounded open set containing the origin that consists of finitely many subdomains such that every subdomain is simply connected and its boundary is connected. The points $\boldsymbol{z}_l \in \mathbb{R}^3_-$, $1 \le l \le m$, are called the *positions of the scatterers* and the value of $0 < \delta \le 1$ determines the common order of the *size of the scatterers*. So, the total collection of scatterers takes the form $D_\delta := \bigcup_{l=1}^m (\boldsymbol{z}_l + \delta B_l)$. Throughout, we denote by $\boldsymbol{\nu}$ the unit outward normal to $\partial D_{\delta,l}$ and ∂B_l relative to $D_{\delta,l}$ and B_l, $1 \le l \le m$, respectively. In presence of these scatterers, the incident field $(\boldsymbol{E}^i, \boldsymbol{H}^i)$ induces a *scattered field* $(\boldsymbol{E}^s, \boldsymbol{H}^s)$, which is a radiating solution of Maxwell's equations (2.2) in $\mathbb{R}^3 \setminus \overline{D_\delta}$ subject to the boundary condition

$$\boldsymbol{\nu} \times \boldsymbol{E}^s = -\boldsymbol{\nu} \times \boldsymbol{E}^i \qquad \text{on } \partial D_\delta.$$

Existence and uniqueness of solutions to this direct problem can be treated as, e.g., in [10, 12, 23].

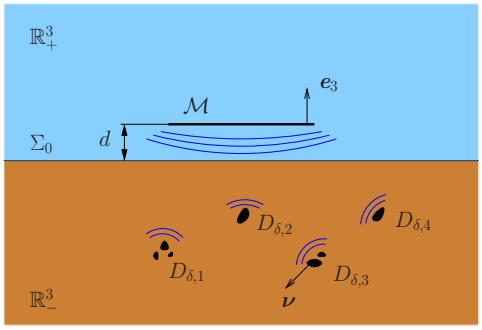

FIGURE 1. Sketch of the geometrical setup.

We shall assume that the measurement device not only imposes the incident fields, but also measures the corresponding scattered magnetic fields $\boldsymbol{H}^s$ on $\mathcal{M}$, cf. Figure 1. The mapping of the imposed dipole density $\boldsymbol{\varphi}$ onto the scattered field $\boldsymbol{H}^s|_{\mathcal{M}}$ defines the *near field measurement operator*

$$G_\delta : L^2(\mathcal{M};\mathbb{C}^3) \to L^2(\mathcal{M};\mathbb{C}^3), \quad G_\delta\boldsymbol{\varphi} := \boldsymbol{H}^s|_{\mathcal{M}}.$$

We study the behavior of G_δ as δ tends to zero, i.e., as the scatterers $D_{\delta,l}$ shrink to the points $\boldsymbol{z}_l$, $l = 1,\dots,m$. More precisely, as the scattered field $\boldsymbol{H}^s|_{\mathcal{M}}$ tends to zero as $\delta \to 0$, we are concerned with the leading order term of $\boldsymbol{H}^s|_{\mathcal{M}}$, which has been determined in [17] analytically. Before we state this result in Theorem 2.2 below we recall the definition and two basic properties of the magnetic and electric polarizability tensors; cf., e.g., Ammari and Kang [3], or Dassios and Kleinman [11]. For this purpose, we need the transpose of the double layer operator $K_{B_l}^{0\top} : H^{-1/2}(\partial B_l;\mathbb{C}) \to H^{-1/2}(\partial B_l;\mathbb{C})$,

$$\big(K_{B_l}^{0\top}\phi\big)(\boldsymbol{x}) := \int_{\partial B_l} \frac{\partial\Phi_0(\boldsymbol{x}-\boldsymbol{y})}{\partial\boldsymbol{\nu}(\boldsymbol{x})}\phi(\boldsymbol{y})\,\mathrm{d}s(\boldsymbol{y}), \qquad \boldsymbol{x}\in\partial B_l,$$

$l = 1,\dots,m$, where Φ_0 is the fundamental solution of the Laplace equation.

DEFINITION 2.1. For B_l, $l = 1,\dots,m$, the *magnetic polarizability tensor* $\mathbb{M}_{B_l}^0 \in \mathbb{R}^{3\times 3}$ is given by

$$\mathbb{M}_{B_l}^0 := -\int_{\partial B_l} \boldsymbol{y}\left(\left(-\frac{1}{2}I + K_{B_l}^{0\top}\right)^{-1}\boldsymbol{\nu}\right)^\top(\boldsymbol{y})\,\mathrm{d}s(\boldsymbol{y})$$

and the *electric polarizability tensor* $\mathbb{M}_{B_l}^\infty \in \mathbb{R}^{3\times 3}$ is given by

$$\mathbb{M}_{B_l}^\infty := \int_{\partial B_l} \boldsymbol{y}\left(\left(\frac{1}{2}I + K_{B_l}^{0\top}\right)^{-1}\boldsymbol{\nu}\right)^\top(\boldsymbol{y})\,\mathrm{d}s(\boldsymbol{y}).$$

The matrices $\mathbb{M}_{B_l}^0$ and $\mathbb{M}_{B_l}^\infty$, $l = 1,\dots,m$, are known to be symmetric and positive definite (cf. Friedman and Vogelius [14], or [3, pp. 91–93]).

THEOREM 2.2. ([16, 17]) *Suppose that $\boldsymbol{\varphi} \in L^2(\mathcal{M};\mathbb{C}^3)$ and $\boldsymbol{H}^i$ is the corresponding incident field from (2.1). Furthermore, denote by $\mathbb{M}_{B_1}^0,\dots,\mathbb{M}_{B_m}^0$ and $\mathbb{M}_{B_1}^\infty,\dots,\mathbb{M}_{B_m}^\infty$ the magnetic and electric polarizability tensors corresponding to*

$B_1, \dots, B_m$, respectively. Then,

$$G_\delta \boldsymbol{\varphi} = \delta^3 \sum_{l=1}^{m} \Big(-k_-^2 \mathbb{G}^m(\cdot, \boldsymbol{z}_l) \mathbb{M}_{B_l}^0 \boldsymbol{H}^i(\boldsymbol{z}_l) + \frac{\mu_-}{\mu_+} \mathbf{curl}_x \mathbb{G}^e(\cdot, \boldsymbol{z}_l) \mathbb{M}_{B_l}^\infty \mathbf{curl} \boldsymbol{H}^i(\boldsymbol{z}_l) \Big) + \mathcal{O}(\delta^4) \tag{2.3}$$

in $L^2(\mathcal{M}; \mathbb{C}^3)$ as $\delta \to 0$. The last term on the right-hand side is bounded by $C\delta^4 \|\boldsymbol{\varphi}\|_{L^2(\mathcal{M};\mathbb{C}^3)}$, where the constant $C > 0$ is independent of δ and $\boldsymbol{\varphi}$.

By (2.3), the scattered magnetic field due to finitely many well separated small perfectly conducting scatterers consists essentially of two terms for each scatterer: The first term $-k_-^2 \mathbb{G}^m(\cdot, \boldsymbol{z}_l) \mathbb{M}_{B_l}^0 \boldsymbol{H}^i(\boldsymbol{z}_l)$, called *magnetic part* below, is the magnetic field of a magnetic dipole at the position of the scatterer $\boldsymbol{z}_l$. The polarization of this dipole is given by the magnetic polarizability tensor times the incident magnetic field at $\boldsymbol{z}_l$. The second term $\frac{\mu_-}{\mu_+} \mathbf{curl}_x \mathbb{G}^e(\cdot, \boldsymbol{z}_l) \mathbb{M}_{B_l}^\infty \mathbf{curl} \boldsymbol{H}^i(\boldsymbol{z}_l)$, called *electric part* below, is the magnetic field of an electric dipole at $\boldsymbol{z}_l$. Its polarization is given by the electric polarizability tensor times the incident electric field at $\boldsymbol{z}_l$. In other words, the dominating term of the expansion (2.3) may be interpreted as the magnetic field on $\mathcal{M}$ due to *fictitious* magnetic and electric sources at the positions $\boldsymbol{z}_l$, $l = 1, \dots, m$.

Following [17] we rewrite (2.3) in operator form as

$$G_\delta = \delta^3 T + \mathcal{O}(\delta^4), \tag{2.4}$$

and note that the leading order term T is an operator of rank $6m$, the range of which is spanned by the columns of $\mathbb{G}^m(\cdot, \boldsymbol{z}_l)$ and $\mathbf{curl}_x \mathbb{G}^e(\cdot, \boldsymbol{z}_l)$, $1 \le l \le m$. Accordingly, if $(\sigma_l, \boldsymbol{u}_l, \boldsymbol{v}_l)_{l=1,\dots,6m}$ denote the singular values and singular vectors of T and $(\sigma_l^\delta, \boldsymbol{u}_l^\delta, \boldsymbol{v}_l^\delta)_{l \in \mathbb{N}}$ the singular values and singular vectors of G_δ (with the singular values in nonincreasing order counting multiplicities), then it follows from classical perturbation theory for linear operators that

$$(\sigma_l^\delta)^2 = \delta^6 \sigma_l^2 + \mathcal{O}(\delta^7), \qquad l \in \mathbb{N}, \tag{2.5}$$

where we have set $\sigma_l = 0$ for $l > 6m$. Due to (2.5) we can say that the left singular vectors of the dominating $6m$ singular values of G_δ span the *essential range* of G_δ.

3. Numerical illustration

In the sequel we illustrate Theorem 2.2 numerically. Our computations correspond to an experimental setup where the measurement device operates on a square $\mathcal{M}$ of size $50 \times 50\,\mathrm{cm}^2$ parallel to the surface of ground, with its center $d = 10\,\mathrm{cm}$ above the origin. The incident fields have a frequency of 20 kHz, corresponding to an angular velocity of $\omega = 1.26 \cdot 10^5\,\mathrm{s}^{-1}$, which is roughly the operating frequency of certain off-the-shelf hand-held metal detectors. Concerning the background medium we will distinguish between vacuum in all of $\mathbb{R}^3$, i.e.,

$$\varepsilon_+ = \varepsilon_- = \varepsilon_0 = 8.85 \cdot 10^{-12}\ \mathrm{Fm}^{-1}, \qquad \mu_+ = \mu_- = \mu_0 = 1.26 \cdot 10^{-6}\ \mathrm{Hm}^{-1},$$

corresponding to $k_+ = k_- = 4.22 \cdot 10^{-4}\,\mathrm{m}^{-1}$ and a wave length of $\lambda_+ = \lambda_- = 14.9\,\mathrm{km}$, and a *two-layered medium* as a more realistic test case for subsurface

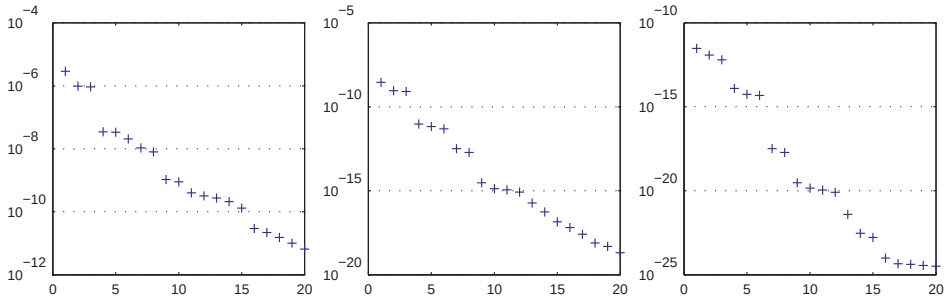

FIGURE 2. Singular values of the measurement operators G_δ from Example 3.1 for $\delta = 1$, $\delta = 10^{-1}$, and $\delta = 10^{-2}$ (from left to right).

exploration, where $\varepsilon_+ = \varepsilon_0$ and $\mu_+ = \mu_0$ as above, and

$$\varepsilon_- = \varepsilon_0\Big(\varepsilon_r + \mathrm{i}\,\frac{\sigma}{\omega\varepsilon_0}\Big) = (0.867 + \mathrm{i}\,59.5)\cdot 10^{-10}\ \mathrm{Fm}^{-1},$$
$$\mu_- = (1+\chi)\mu_0 = 1.26\cdot 10^{-6}\ \mathrm{Hm}^{-1},$$

modelling air and soil, respectively. The particular electromagnetic soil parameters $\sigma = 7.5\cdot 10^{-4}\ \mathrm{Sm}^{-1}$, $\chi = 1.9\cdot 10^{-5}$, and $\varepsilon_r = 9.8$ refer to a poor clay sand, cf. Igel and Preetz [21]. The wave number for the soil is $k_- = (7.77 + \mathrm{i}\,7.66)\cdot 10^{-3}\,\mathrm{m}^{-1}$, corresponding to a wave length of $\lambda_- = 0.81$ km. In either case the wave length we experience is larger by many orders of magnitude than the scattering obstacles that we are looking for.

In practice we only have a finite amount of incident fields and a discrete set of measurements of the corresponding scattered fields. We assume that measurements of the scattered fields $\boldsymbol{H}^s$ are available for all points of a regular square $n \times n$ grid $\mathcal{M}_h \subset \mathcal{M}$ with mesh width h, and that every mesh point $\boldsymbol{y} \in \mathcal{M}_h$ and each of the three Cartesian coordinate directions $\boldsymbol{e}_j$, $j = 1, 2, 3$, is used to generate an incident field $\boldsymbol{H}^i = k_+^2 \mathbb{G}^m(\cdot, \boldsymbol{y})\boldsymbol{e}_j$ of a magnetic dipole in $\boldsymbol{y}$ with polarization $\boldsymbol{e}_j$. In our examples, we use $n = 6$ and, accordingly, $h = 10\,\mathrm{cm}$. An appropriate ordering of these data in a 108×108 matrix $G_{\delta,h}$ is known as the *multistatic response matrix*, cf., e.g., [13].

EXAMPLE 3.1. To illustrate Theorem 2.2 we generate data for a perfectly conducting small ellipsoidal scatterer $D_\delta = \boldsymbol{z} + \delta B$, $0 < \delta \leq 1$, in vacuum, sitting 20 cm below the origin. The semi axes of B are aligned with the coordinate axes and are 9, 7, and 5 cm long, respectively.

Figure 2 shows the corresponding 20 largest singular values of the resulting multistatic response matrices, using three values of δ ranging from $\delta = 1$ over $\delta = 10^{-1}$ down to $\delta = 10^{-2}$. According to (2.5), we expect to see 6 singular values of order $\mathcal{O}(\delta^3)$, while the remaining singular values should be of order $\mathcal{O}(\delta^4)$. In fact, the six dominating singular values, which are of the order 10^{-5} down to 10^{-8} for $\delta = 1$ are, roughly, reduced by six orders of magnitude for $\delta = 10^{-2}$, which is exactly as predicted by the theory. Beginning with the seventh singular value (of the order 10^{-8} for $\delta = 1$) the reduction is significantly stronger, namely nine and more orders of magnitude. For $\delta = 10^{-2}$ the gap between the dominating six and the remaining singular values is very distinct.

We mention that the results are much alike for the two-layered medium, although the separation of the dominating six singular values is less pronounced in that case. We refer to [16, pp. 91–93] for details and visualizations. □

As a general rule we have found in all our numerical experiments that the dominating 6 singular values come in two close triples that are well separated from each other: In Figure 2, for example, the two triples are separated by about two orders of magnitude, essentially independent of the value of δ. This separation is due to the fact that our wave length is much larger than the distance between the scatterer and the measurement device. To understand this somewhat better we provide an analytical example.

EXAMPLE 3.2. Denote by B the unit sphere and assume that a perfectly conducting sphere shaped scatterer $D_\delta = \boldsymbol{z} + \delta B$ is buried at position $\boldsymbol{z}$ in a homogeneous background medium. The incident field is generated by a single magnetic dipole with polarization $\boldsymbol{p}$ at the origin, i.e., $\boldsymbol{H}^i = k^2\mathbb{G}(\cdot,\mathbf{0})\boldsymbol{p}$ and $\boldsymbol{E}^i = \mathrm{i}\,\omega\mu\mathbf{curl}_x\mathbb{G}(\cdot,\mathbf{0})\boldsymbol{p}$, where $\mathbb{G}$ denotes the dyadic Green's function for Maxwell's equations in the homogeneous background medium. (For homogeneous media the magnetic and electric dyadic Green's function coincide.) The magnetic and the electric polarizability tensors for the unit sphere B are given by $\mathbb{M}_B^0 = 2\pi\mathbb{I}_3$ and $\mathbb{M}_B^\infty = 4\pi\mathbb{I}_3$, respectively (cf. [3]). According to (2.3) the scattered field in the origin is given by

$$\boldsymbol{H}^s(\mathbf{0}) = -\delta^3\big(2\pi k^4\mathbb{G}(\boldsymbol{z},\mathbf{0})\mathbb{G}(\boldsymbol{z},\mathbf{0})\boldsymbol{p} + 4\pi k^2\mathbf{curl}_x\mathbb{G}(\boldsymbol{z},\mathbf{0})\mathbf{curl}_x\mathbb{G}(\boldsymbol{z},\mathbf{0})\boldsymbol{p}\big) + \mathcal{O}(\delta^4).$$

To estimate the magnetic and the electric part of the leading order term in this asymptotic expansion, we recall the explicit form of the dyadic Green's function for the homogeneous medium,

$$\mathbb{G}(\boldsymbol{z},\mathbf{0}) = \Phi_k(\boldsymbol{z})\mathbb{I}_3 + \frac{1}{k^2}\nabla_x\,\mathrm{div}_x(\Phi_k(\boldsymbol{z})\mathbb{I}_3), \qquad \boldsymbol{z}\neq\mathbf{0}, \tag{3.1}$$

where $\Phi_k(\boldsymbol{z}) = e^{\mathrm{i}\,k|\boldsymbol{z}|}/(4\pi|\boldsymbol{z}|)$ denotes the fundamental solution of the Helmholtz equation (cf., e.g., [23]). A short calculation shows that

$$\begin{aligned}\mathbb{G}(\boldsymbol{z},\mathbf{0}) = \Phi_k(\boldsymbol{z})\mathbb{I}_3 - \Phi_k(\boldsymbol{z})\frac{1}{|\boldsymbol{z}|^2}\begin{pmatrix} z_1z_1 & z_1z_2 & z_1z_3\\ z_1z_2 & z_2z_2 & z_2z_3\\ z_1z_3 & z_2z_3 & z_3z_3\end{pmatrix}\\ + \frac{1}{k^2}\Big(\mathrm{i}\,k - \frac{1}{|\boldsymbol{z}|}\Big)\Phi_k(\boldsymbol{z})\frac{1}{|\boldsymbol{z}|^3}\begin{pmatrix} -2z_1^2+z_2^2+z_3^2 & -3z_1z_2 & -3z_1z_3\\ -3z_1z_2 & z_1^2-2z_2^2+z_3^2 & -3z_2z_3\\ -3z_1z_3 & -3z_2z_3 & z_1^2+z_2^2-2z_3^2\end{pmatrix}\end{aligned}$$

and

$$\mathbf{curl}_x\mathbb{G}(\boldsymbol{z},\mathbf{0}) = \Big(\mathrm{i}\,k - \frac{1}{|\boldsymbol{z}|}\Big)\Phi_k(\boldsymbol{z})\frac{1}{|\boldsymbol{z}|}\begin{pmatrix} 0 & -z_3 & z_2\\ z_3 & 0 & -z_1\\ -z_2 & z_1 & 0\end{pmatrix}.$$

Assuming that $k|\boldsymbol{z}| \ll 1$, we expand $\frac{1}{k}\Phi_k(\boldsymbol{z})$, $\frac{1}{k}\mathbb{G}(\boldsymbol{z},\boldsymbol{0})$, and $\frac{1}{k^2}\mathbf{curl}_x\mathbb{G}(\boldsymbol{z},\boldsymbol{0})$ in terms of k and obtain that

$$\begin{aligned}
\frac{1}{k}\Phi_k(\boldsymbol{z}) &= \frac{1}{4\pi k|\boldsymbol{z}|} + \frac{\mathrm{i}}{4\pi} - \frac{k|\boldsymbol{z}|}{8\pi} + \mathcal{O}\big((k|\boldsymbol{z}|)^2\big),\\
\frac{1}{k}\mathbb{G}(\boldsymbol{z},\boldsymbol{0}) &= -\frac{1}{4\pi(k|\boldsymbol{z}|)^3}\frac{1}{|\boldsymbol{z}|^2}\begin{pmatrix} -2z_1^2+z_2^2+z_3^2 & -3z_1z_2 & -3z_1z_3\\ -3z_1z_2 & z_1^2-2z_2^2+z_3^2 & -3z_2z_3\\ -3z_1z_3 & -3z_2z_3 & z_1^2+z_2^2-2z_3^2\end{pmatrix}\\
&\quad + \mathcal{O}\Big(\frac{1}{k|\boldsymbol{z}|}\Big),
\end{aligned}$$

and

$$\frac{1}{k^2}\mathbf{curl}_x\mathbb{G}(\boldsymbol{z},\boldsymbol{0}) = -\frac{1}{4\pi(k|\boldsymbol{z}|)^2}\frac{1}{|\boldsymbol{z}|}\begin{pmatrix} 0 & -z_3 & z_2\\ z_3 & 0 & -z_1\\ -z_2 & z_1 & 0\end{pmatrix} + \mathcal{O}(1).$$

Thus, the magnetic part of the scattered magnetic field satisfies

$$\begin{aligned}
&-2\pi k^4\mathbb{G}(\boldsymbol{z},\boldsymbol{0})\mathbb{G}(\boldsymbol{z},\boldsymbol{0})\boldsymbol{p}\\
&= -k^6\Bigg(\frac{1}{8\pi(k|\boldsymbol{z}|)^6}\frac{1}{|\boldsymbol{z}|^4}\begin{pmatrix} -2z_1^2+z_2^2+z_3^2 & -3z_1z_2 & -3z_1z_3\\ -3z_1z_2 & z_1^2-2z_2^2+z_3^2 & -3z_2z_3\\ -3z_1z_3 & -3z_2z_3 & z_1^2+z_2^2-2z_3^2\end{pmatrix}^2\boldsymbol{p}\\
&\qquad + \mathcal{O}\Big(\frac{1}{(k|\boldsymbol{z}|)^4}\Big)\Bigg),
\end{aligned}$$

and the electric part of the scattered magnetic field fulfills

$$\begin{aligned}
&-4\pi k^2\mathbf{curl}_x\mathbb{G}(\boldsymbol{z},\boldsymbol{0})\mathbf{curl}_x\mathbb{G}(\boldsymbol{z},\boldsymbol{0})\\
&\qquad = -k^6\Bigg(\frac{1}{4\pi(k|\boldsymbol{z}|)^4}\frac{1}{|\boldsymbol{z}|^2}\begin{pmatrix} 0 & -z_3 & z_2\\ z_3 & 0 & -z_1\\ -z_2 & z_1 & 0\end{pmatrix}^2\boldsymbol{p} + \mathcal{O}\Big(\frac{1}{(k|\boldsymbol{z}|)^2}\Big)\Bigg).
\end{aligned}$$

Since we have assumed $k|\boldsymbol{z}| \ll 1$, it follows that

$$\frac{1}{(k|\boldsymbol{z}|)^4} \ll \frac{1}{(k|\boldsymbol{z}|)^6},$$

and hence, the magnetic part of the scattered magnetic field is significantly larger than the electric part (for low frequencies and in the near field). □

As we have thus seen, for our very small frequencies the magnetic part of the scattered field can be expected to dominate the electric part of the field. Since the essential range of G_δ is close to the range of T, which is spanned by the columns of $\mathbb{G}^m(\cdot,\boldsymbol{z})$ and $\mathbf{curl}_x\mathbb{G}^e(\cdot,\boldsymbol{z})$, respectively, this suggests that the three dominating singular values correspond to the magnetic part, i.e. that the corresponding left singular vectors span the columns of $\mathbb{G}^m(\cdot,\boldsymbol{z})$.

In fact, this can be verified numerically. To this end we compute the left singular vectors for the three dominating singular values of the multistatic response matrix of Example 3.1 with parameter $\delta = 0.01$ (corresponding to the right-most plot in Figure 2). As a result we see that the angle between the span of the columns of the magnetic dyadic Green's function $\mathbb{G}^m(\cdot,\boldsymbol{z})$ and any of these three singular vectors is below 0.016.

Although it is tempting to believe that the second triple of singular values now corresponds to the electric part of the scattered field, the latter is not entirely true. In fact, if this were correct then the analysis of Example 3.2 would indicate that the two triples are separated by, roughly, $\mathcal{O}((k|\boldsymbol{z}|)^2)$, which corresponds to 10^{-8}, approximately, and not to 10^{-2} as in Figure 2. Note that the singular vectors corresponding to the second triple can only belong to the electric part of the scattered field if the electric part is orthogonal to the magnetic part. This, however, is not true in general, as has been demonstrated analytically in [1, 19] for a homogeneous as well as a two-layered background medium, and in greatest detail in [20] for the homogeneous case. Accordingly, the singular vectors do not split exactly in magnetic and electric ones, and as a consequence, the gap between the two triples in Figure 2 is not as large as one might expect from the estimate in Example 3.2.

4. A MUSIC-type reconstruction method for the inverse problem

Similar to [7], the asymptotic formula (2.3) can be used to justify a MUSIC-type reconstruction method suggested independently by Iakovleva, Lesselier, et al. in [1, 19].

To this end we recall that T of (2.4) is an operator of rank $6m$ whose range is spanned by the columns of $\mathbb{G}^m(\cdot, \boldsymbol{z}_l)$ and $\mathbf{curl}_x \mathbb{G}^e(\cdot, \boldsymbol{z}_l)$, $1 \le l \le m$. Vice versa, using the unique continuation and reflection principles one can show that the dipole function

$$\boldsymbol{g}_{y,d} := \big(\mathbb{G}^m(\cdot, \boldsymbol{y})\boldsymbol{d}_1 + \mathbf{curl}_x \mathbb{G}^e(\cdot, \boldsymbol{y})\boldsymbol{d}_2\big)\big|_{\mathcal{M}} \tag{4.1}$$

with $\boldsymbol{y} \in \mathbb{R}^3_-$ and $\boldsymbol{d} = (\boldsymbol{d}_1, \boldsymbol{d}_2) \in \mathbb{C}^3 \times \mathbb{C}^3 \setminus (0, 0)$ belongs to the range $\mathcal{R}(T)$ of T, if and only if $\boldsymbol{y} \in \{\boldsymbol{z}_1, \dots, \boldsymbol{z}_m\}$, cf. [17, Prop. 9.3].

If P denotes the orthogonal projector on $\mathcal{R}(T)$ and $\beta(\boldsymbol{y})$ the angle between $\boldsymbol{g}_{y,d}$ and $\mathcal{R}(T)$ then

$$\cot \beta(\boldsymbol{y}) = \frac{\|P\boldsymbol{g}_{y,d}\|_{\boldsymbol{L}^2(\mathcal{M};\mathbb{C}^3)}}{\|(I-P)\boldsymbol{g}_{y,d}\|_{\boldsymbol{L}^2(\mathcal{M};\mathbb{C}^3)}},$$

and this cotangent gets large, if the angle between $\boldsymbol{g}_{y,d}$ and the range of T is small. In particular, we have

$$\boldsymbol{y} \in \{\boldsymbol{z}_l \mid l = 1, \dots, m\} \iff \beta(\boldsymbol{y}) = 0 \iff \cot \beta(\boldsymbol{y}) = \infty. \tag{4.2}$$

In view of (2.4) the projector P on $\mathcal{R}(T)$ is essentially the same for small values of δ as the projector

$$P^\delta_{6m} : \boldsymbol{L}^2(\mathcal{M}; \mathbb{C}^3) \to \operatorname{span}_{\mathbb{C}}\{\boldsymbol{u}^\delta_1, \dots, \boldsymbol{u}^\delta_{6m}\}$$

on the essential range of G_δ. With the given data we may therefore replace P by P^δ_{6m}, and approximate

$$\cot \beta(\boldsymbol{y}) \approx \frac{\|P^\delta_{6m}\boldsymbol{g}_{y,d}\|_{\boldsymbol{L}^2(\mathcal{M};\mathbb{C}^3)}}{\|(I-P^\delta_{6m})\boldsymbol{g}_{y,d}\|_{\boldsymbol{L}^2(\mathcal{M};\mathbb{C}^3)}} =: \cot \beta^\delta_{6m}(\boldsymbol{y}). \tag{4.3}$$

In view of (4.2) we therefore expect to see large values of $\cot \beta^\delta_{6m}(\boldsymbol{y})$ for test points $\boldsymbol{y} \in \mathbb{R}^3_-$ which are close to the points $\boldsymbol{z}_l$, $l = 1, \dots, m$.

It remains to determine the parameter $m \in \mathbb{N}$, i.e., the unknown number of scatterers. According to (2.5) this amounts to estimate the dimension of the essential range of G_δ, i.e., to search for a reasonable gap in its singular values. Whether this works in practice, strongly depends on the amount of noise in the data and on the particular configuration of the scatterers.

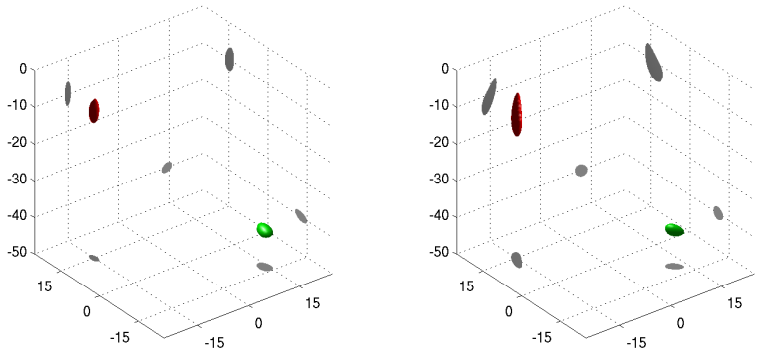

FIGURE 3. "Two-layered" reconstruction from Example 4.1 (left) vs. "homogeneous" reconstruction from Example 4.2 (right).

Alternatively, one can visualize color coded plots of the cotangent $\cot \beta_l^\delta$ of (4.3) for a sequence of increasing subspace dimensions $l = 6, 12, 18, \ldots$. Note that the fraction in the middle of (4.3) is monotonically increasing with l, and typically, the number of reconstructed scatterers is also increasing with l until all the scatterers have been found. This strategy from [7] has worked well in all our numerical examples.

Concerning the discrete setting with a finite grid and corresponding multistatic response matrix, it has been shown by Kirsch [22, Thm. 2.1] (see also [1, Prop. 6.3]) that for a fixed number m of scatterers the range characterization (4.2) carries over to this discrete setting, provided that the number n^2 of grid points is sufficiently large. Our numerical experience suggests that in practice fairly small numbers n already suffice for this purpose, e.g., $n^2 = 9$ in case of $m = 2$ scatterers. As a consequence, the singular value decomposition of the mulistatic response matrix is usually cheap to compute.

Due to the reciprocity principle the multistatic response matrix should be complex symmetric with respect to the proper discrete inner product. However, due to noise in the data the given matrix fails to do so in general. On the other hand, the size of this failure can be used to estimate the noise in the data and the reliability of the computed singular values, compare [15, Sect. 7]. Only those singular values that stick out of this noise level can be considered reliable.

At this point we emphasize that the singular values of G decay superlinearly to zero and therefore, in the presence of noise the given data contain only very limited information about the scatterers: the inverse obstacle problem is *ill-posed*, cf., e.g., Colton and Kress [9]. The a priori information we use, though, i.e., the smallness of the scatterers, stabilizes the problem because most of the information that is required to restore the positions $\boldsymbol{z}_l$, $l = 1, \ldots, m$, is encoded in the dominating $6m$ singular values, only.

EXAMPLE 4.1. A first numerical example of the MUSIC-type implementation described above has already been presented in [17], where a reconstruction has been shown of two small perfectly conducting ellipsoidal obstacles, with semi axes

of length $(0.1, 0.2, 0.3)$ cm and $(2, 3, 1)$ cm, respectively, buried in the lower halfspace (the soil) of the two-layered background medium described in Section 3, see also the left-hand plot of Figure 3. The centers of the two ellipsoids are at the positions $(-15, 15, -10)$ cm and $(15, -15, -40)$ cm, respectively. The forward data for this example contain an estimated numerical error of 4%, and some additional (uniformly distributed) random noise of about 3%. Our MUSIC-type reconstruction is based on the test function (4.1) with polarization vector $\boldsymbol{d} = (\boldsymbol{e}_3, \boldsymbol{e}_3)$ and recovers the position of both scatterers, it even indicates the orientation of the ellipsoidal objects. Note that the plot in Figure 3 not only visualizes the reconstructed positions of the two scatterers but also their projections onto the boundaries of the box to enhance the three dimensional perspective.

Figure 3 differs from the one in [17], as different isosurfaces are shown in different areas of the region of interest: The component of the isosurface showing the upper obstacle corresponds to $\cot \beta_{12}^{\delta}(\boldsymbol{y}) = 25$, whereas the other one uses the value $\cot \beta_{12}^{\delta}(\boldsymbol{y}) = 125$. This is one of the major advantages of these MUSIC-type methods, that the choice of the test points $\boldsymbol{y}$ as well as their density can be steered adaptively, which can be utilized to zoom in on relevant parts of the region of interest. □

For the two-layered medium the time consuming part of the inversion process consists in the evaluation of the test functions $\boldsymbol{g}_{y,d}$ on the grid $\mathcal{M}_h$ for each sampling point $\boldsymbol{y}$ in the region of interest. According to (4.1) these test functions are superpositions of magnetic dyadic Green's functions and the curls of electric dyadic Green's functions for the two-layered medium, which are not known in closed form, but only via Hankel transforms. So, the computation of $\boldsymbol{g}_{y,d}$ requires the evaluation of these Hankel transforms, for which we have used an implementation which goes back to Anderson [5], and which has been made available on the web by Borchers [6]. On the other hand, the dyadic Green's function for the homogeneous background medium is known explicitly, cf. (3.1), and can be implemented efficiently.

Our numerical experiments indicate (see Schneider [24] for an analytical justification) that in the low frequency regime which is considered here, the Green's functions for the air/soil layered medium do not differ very much from the Green's functions for air alone. Thus, we can use the test function

$$\boldsymbol{g}_{y,d}^{hom} := \big(\mathbb{G}(\cdot, \boldsymbol{y})\boldsymbol{d}_1 + \mathbf{curl}_x \mathbb{G}(\cdot, \boldsymbol{y})\boldsymbol{d}_2\big)\big|_{\mathcal{M}} \tag{4.4}$$

instead of (4.1) for an implementation of the MUSIC-type inversion.

Example 4.2. For a numerical illustration we pick the same example as before, but now use the *homogeneous* test function (4.4) (with the same polarization vector $\boldsymbol{d} = (\boldsymbol{e}_3, \boldsymbol{e}_3)$ as above) for the reconstruction. The right-hand side plot of Figure 3 shows the corresponding reconstruction and allows a comparison with the reconstruction obtained with the correct test function (4.1). (The isosurface values are somewhat smaller here, namely 20 and 85 instead of the values 25 and 125 that have been used above.) Both variants of the algorithm detect the two scatterers at about the correct location, but for this simplified algorithm here, the orientation that is shown in the plot is not the real one. This can also be seen from the color coded plots of horizontal cross sections of $\cot \beta_{12}^{\delta}$ in Figure 4. For these plots the cotangents have been evaluated for all sampling points on an equidistant grid with mesh width 0.5 cm only. While the two plots in the top row correspond to the original version with the two-layered test function (4.1), the bottom row shows the

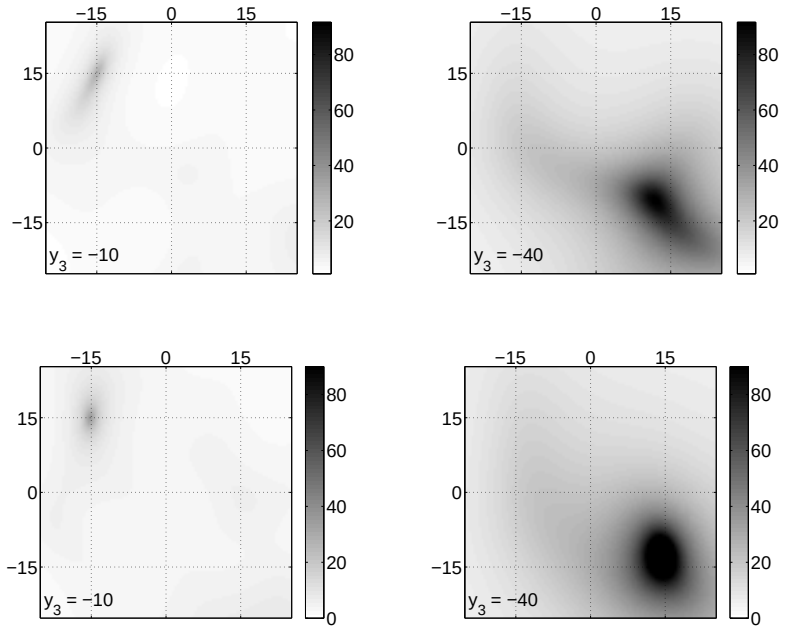

FIGURE 4. Cross-sectional plots of $\cot \beta_{12}^{\delta}(\boldsymbol{y})$ for the "homogeneous" reconstruction from Example 4.2 (top row) vs. the "two-layered" reconstruction from Example 4.1 (bottom row) at $y_3 = -10\,\mathrm{cm}$ (left) and $y_3 = -40\,\mathrm{cm}$ (right).

corresponding plots for the homogeneous test function (4.4) that has been used in the present example. In both rows the left-hand plot refers to the horizontal cross section at $y_3 = -10\,\mathrm{cm}$, whereas the right-hand plot shows the cross section for $y_3 = -40\,\mathrm{cm}$. For ease of comparison we have used the same color codes in all four plots; we remark, however, that with the two-layered test function (4.1) the peak of $\cot \beta_{12}^{\delta}$ at the lower cross section $y_3 = -40\,\mathrm{cm}$ is much more significant than for the homogeneous test function.

In summary, the reconstruction with the correct two-layered test function is somewhat better, but the computation of the other reconstruction has been about 85 times faster. □

Naturally, one should also investigate the limitations of the method. For example, one may ask: How many obstacles can be determined simultaneously this way? The answer depends on various parameters, the obvious ones being size, depth, and noise.

Because of the ill-posedness of the problem, the crucial point here is the noise level, whereas the actual number of obstacles does not appear to be very important. As mentioned before, only those singular values that are above the noise level carry reliable information about the scatterers. On the other hand, the signal sent back from the scatterers diminishes with their distance to the measuring device, and thus, falls below the noise level from some distance onwards. At the same time, as

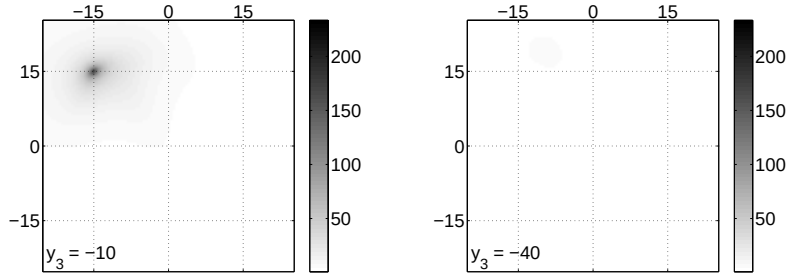

FIGURE 5. Cross-sectional plots of $\cot \beta_{12}^{\delta}(\boldsymbol{y})$ at $y_3 = -10$ cm and $y_3 = -40$ cm for Example 4.3.

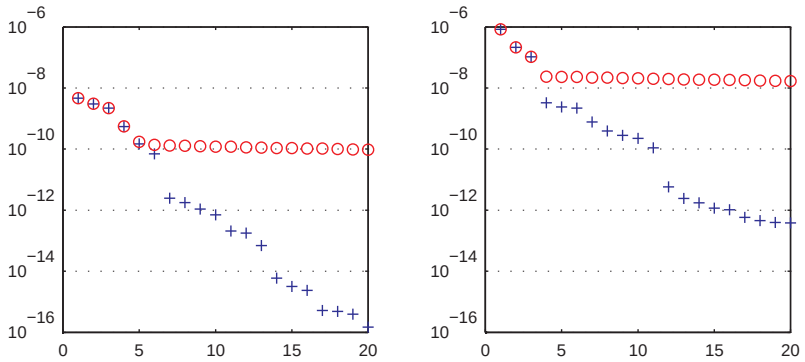

FIGURE 6. Singular values of the measurement operators G_δ ($+$ without additional noise, $\circ$ with 3% uniformly distributed noise) for the configuration from Example 4.1 (left) and the one from Example 4.3 (right).

is seen from Theorem 2.2, the magnitude of this signal decreases with the diameter δ of the scatterer, and therefore small scatterers will again be hidden in the noise.

EXAMPLE 4.3. To illustrate this observation we slightly modify the geometrical setup from Example 4.1 and enlarge the upper scatterer at position $(-15, 15, -10)$ cm by a factor of ten. The simulated data for this example contain an estimated numerical error of 2%, and additionally we perturb these data by a uniformly distributed relative error of 3%, as in Example 4.1. For the reconstruction we also use the same parameters in our implementation as in Example 4.1. Figure 5 shows the resulting horizontal cross sections of $\cot \beta_{12}^{\delta}(\boldsymbol{y})$ for $y_3 = -10$ cm and $y_3 = -40$ cm, which should be compared with the plots in the bottom row of Figure 4. Note that no improvement of the right-hand side plot of Figure 5 is possible by using other color codes, and hence, only the position of the upper scatterer can be estimated from these plots.

To explain this result we conclude from the asymptotic formula (2.3) that the magnitude of the fictitious source in the upper scatterer is approximately 1000 times larger here than in Example 4.1, because the diameter of this scatterer has been

increased by a factor of 10. In fact, the dominating singular values have jumped up from about 10^{-8} up to 10^{-6}, as can be seen from the crosses in Figure 6. As the noise level is relative to the size of the signal, this level has also increased by slightly more than two orders of magnitude. On the other hand, the intensity of the fictitious source in the other scatterer remains essentially the same, and therefore disappears in the noise, cf. the circles in Figure 6: While six singular vectors have carried information in Example 4.1, only three of them are useful here.

In fact, we may take another step in our interpretation of Figure 6 on the grounds of Section 3. According to the analysis in Section 3 we may guess that the six dominating singuar values in the left-hand plot of Figure 6 carry information about the magnetic parts of the scattered fields from the two scatterers. In the light of the two plots in the bottom row of Figure 4 the intensity of the fictitious source in the lower scatterer is stronger than the other one. Therefore the dominating singular value triple will most likely correspond to the lower scatterer and the second triple is associated with the upper one: In fact, this second triple has increased by three orders of magnitude whereas the other triple remained near 10^{-8}, as can be seen from the crosses in the right-hand side plot of Figure 6. It is also possible to see that the non-magnetic singular value triple of the upper scatterer has also been raised by three orders of magnitude, from 10^{-12} up to 10^{-9}. □

5. Superresolution

Finally, we investigate the spatial resolution of our MUSIC-type reconstruction algorithm. The usual expectation from the engineering literature concerning the achievable spatial resolution would be based on the celebrated Nyquist criterion, which says that this spatial resolution is linked to the frequency, i.e., two scattering obstacles can be identified as separate objects if their distance is above the wave length of the signal, which, in our case, amounts to kilometers. It has already been observed by Devaney [13], who coined the term *superresolution* for this phenomenon, that the resolution of MUSIC-type inversion methods can be better than that and, as we have seen in Example 4.1, the resolution of our algorithm is even superior by orders of magnitude.

To pin down the available resolution we study the following benchmark problem, which uses the same measurement setup as before, although we confine ourselves to the homogeneous background medium for the ease of simplicity. We consider two perfectly conducting spheres with radius 1 cm that are buried 20 cm underneath the measurement device at positions $(-a/2, 0, -10)$ and $(a/2, 0, -10)$ cm, respectively, i.e., the two spheres are a centimeters apart. The forward data for this example contain estimated numerical errors of about 1.3%. For the reconstruction we again use the test function (4.4) with polarization vector $\boldsymbol{d} = (\boldsymbol{e}_3, \boldsymbol{e}_3)$, and to visualize our reconstructions we look at the values of $\cot \beta_{12}^{\delta}(\boldsymbol{y})$ in the horizontal cross section $y_3 = -10$ cm which contains the two scatterers.

Example 5.1. In our first example, we vary the distance a from 5 to 20 cm and perturb the resulting multistatic response matrices by 1% uniformly distributed random noise. Figure 7 shows the corresponding reconstructions, in which the two small circles indicate the true positions and the size of the scatterers. We observe that for $a \geq 12.5$ cm the two scatterers can be perfectly distinguished in these reconstructions. Beginning with $a = 10$ cm the reconstructions of the two scatterers start getting smeared out until they merge, eventually: For $a = 5$ cm and below

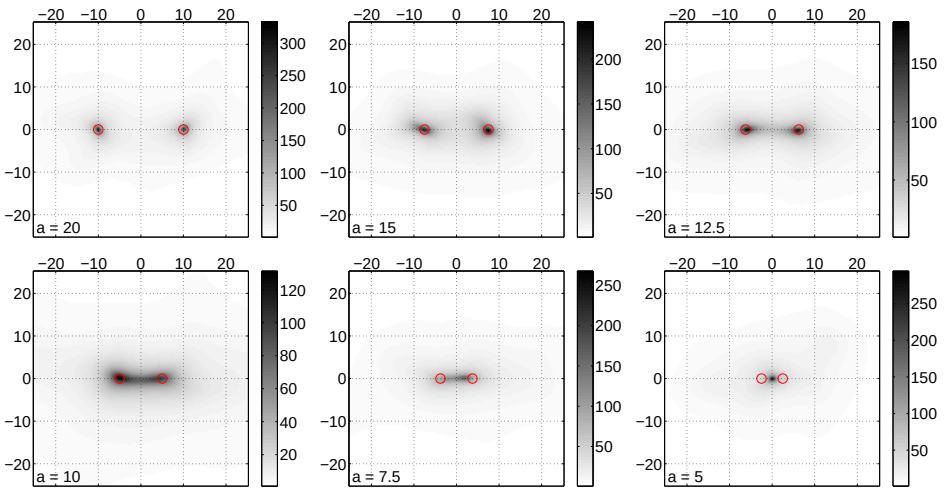

FIGURE 7. Cross-sectional plots of $\cot \beta_{12}^{\delta}$ for 1% noise, from $a = 20\,\text{cm}$ (top left) down to $a = 5\,\text{cm}$ (bottom right).

the reconstructions only show one single object situated in the center of mass of the two true obstacles. □

For this particular example we thus have observed a resolution between 5 and 10 cm (at 20 cm below the measurement device), which is around 7 orders of magnitude smaller than the wave length. We truly see some kind of superresolution. As in Example 4.3, however, this resolution depends on the quality of the data, i.e., on the noise level. In the next example we therefore investigate the influence of noise.

EXAMPLE 5.2. In Figure 8 we show the singular values of the multistatic response matrices corresponding to distances a between 5 and 20 cm again, with three different noise levels in each plot. For $a = 20\,\text{cm}$ the first 6 singular values which we expect to correspond to the magnetic parts of the scattered fields from the two scatterers, are clearly separated from the others. When the distance between the two scatterers is reduced, the second triple of singular values gets smaller and smaller. Recalling the results of Example 5.1 we see a coincidence between the loss of resolution experienced there and the immersion of the second triple of singular values into the noise level. When only three singular values are beyond this level then only one object is reconstructed at the center of mass.

Based on this observation we expect to see a spatial resolution of about 5 cm with 0.3% additive noise, whereas the spatial resolution should increase up to more than 12.5 cm with 3% noise. This is, in fact, nicely illustrated in Figures 9 and 10 which show the corresponding reconstructions. □

To explain these results somewhat further we first observe that according to Theorem 2.2 the measured field is, up to first order, the superposition of two fictitious sources in the two obstacles. As each of these scatterers/sources approaches the same point underneath the origin, the corresponding fields, which depend continously on the locations of the scatterers, both converge to the field of a fictitious

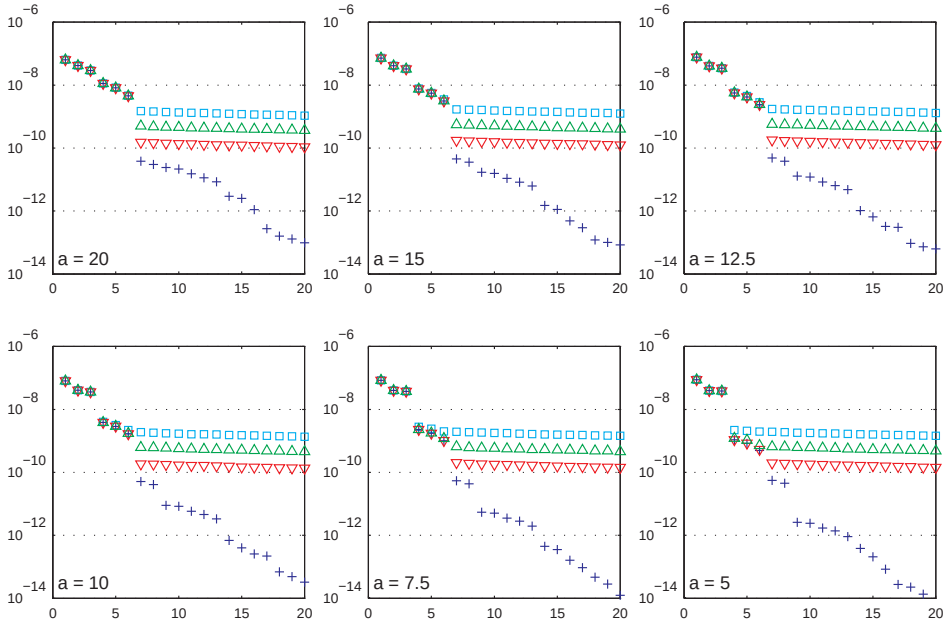

FIGURE 8. Singular values of the measurement operators G_δ ($+$ without additional noise, $\triangledown$ with 0.3% uniformly distributed noise, $\triangle$ with 1% uniformly distributed noise, $\square$ with 3% uniformly distributed noise).

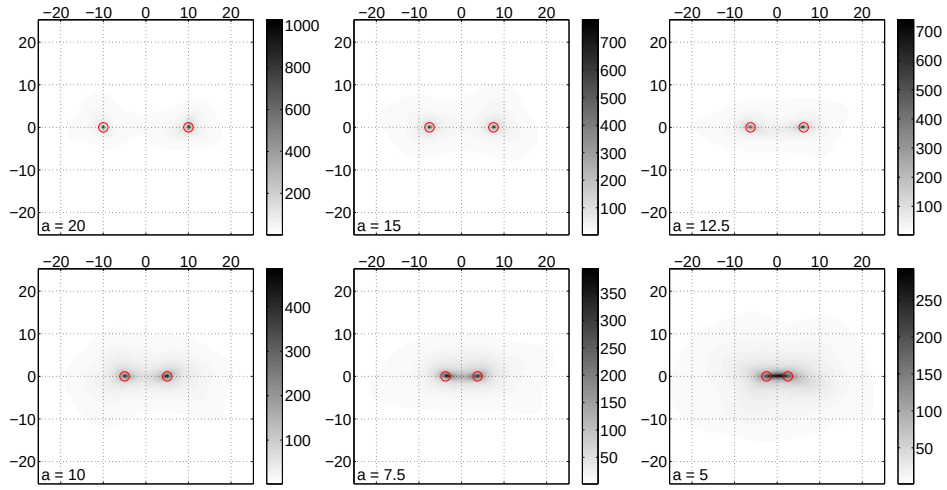

FIGURE 9. Cross-sectional plots of $\cot \beta_{12}^\delta$ for 0.3% noise, from $a = 20\,\mathrm{cm}$ (top left) down to $a = 5\,\mathrm{cm}$ (bottom right).

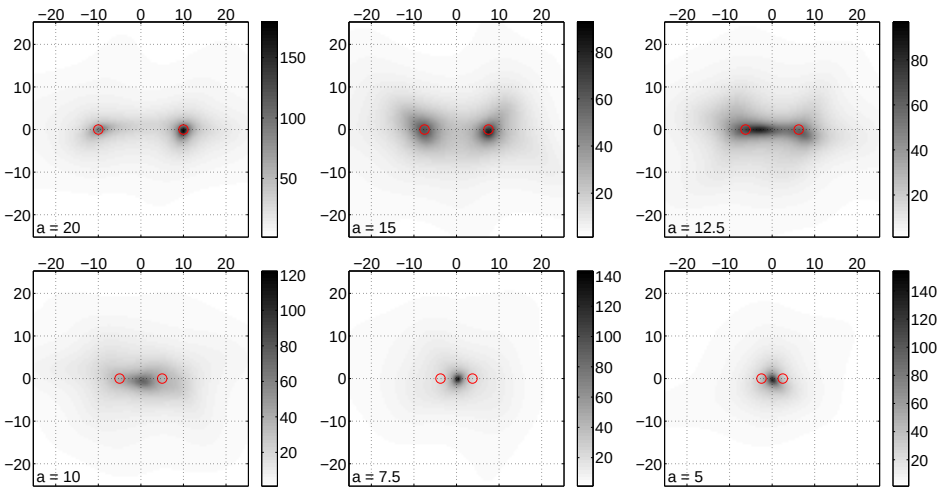

FIGURE 10. Cross-sectional plots of $\cot \beta_{12}^{\delta}$ for 3% noise, from $a = 20\,\text{cm}$ (top left) down to $a = 5\,\text{cm}$ (bottom right).

source underneath the origin. The dimension of the essential range of the multistatic response matrix will therefore drop down to three as $a \to 0$, corresponding to the span of the magnetic part of the scattered field due to one fictitious scatterer underneath the origin. This is what we see from the crosses in Figure 8, and as soon as the fourth singular value has immerged into the noise level, the MUSIC-type algorithm is fooled because all the remaining significant singular vectors correspond to this new fictitious obstacle.

To conclude, we briefly address the question whether the available resolution depends on the distance between the receivers, i.e., the mesh width h of the grid $\mathcal{M}_h$. As we have mentioned before, the results in [22, Thm. 2.1] (see also [1, Prop. 6.3]) may be used to argue that the performance of the MUSIC-type algorithm should be quite independent of the discretization $\mathcal{M}_h$ of the measurement device $\mathcal{M}$, as long as the number of grid points is sufficiently large to obtain enough singular vectors needed for the reconstruction.

We have confirmed this numerically by varying the mesh width h of the discrete measurement device. We can report that for an equidistant 21×21 grid with mesh width $h = 2.5\,\text{cm}$ and a 3×3 grid with mesh width $h = 25\,\text{cm}$ the reconstructions and their resolutions have been essentially the same as above, which shows that the resolution is pretty independent of the number of grid points and the mesh width of the measurement device.

We finally mention that we have discussed only one single case study to shed some light on the resolution of the MUSIC-type algorithm, and this certainly does not cover all possible situations of interest. Other investigations related to the resolution limit of MUSIC-type algorithms can be found, e.g., in Ammari et al. [4], see also [1, p. 706].

Conclusion

We have shown for a specific problem of subsurface imaging that the multistatic response matrix corresponding to time-harmonic electromagnetic scattering can be used to reconstruct tiny obstacles in the ground, as long as the relevant information is above the inherent noise in the data. We also have examplified that it is this noise level and not a signal processing type restriction like the Nyquist bound that ultimately limitates the resolution of our MUSIC-type reconstructions, although the recovery of such a resolution is a severely ill-posed problem. For the low frequencies in our application we have seen that the magnetic part of the asymptotic formula (2.3) is dominating the corresponding electric part, and we have discussed how this affects our numerical results.

Acknowledgments

This work has been supported by the German Federal Ministery of Education and Research (BMBF) under grant 01 TX 0302.

The authors are pleased to thank Roland Potthast and his group for providing their codes from [12] to generate the forward data for the numerical examples, and to thank Christoph Schneider for making his code from [15] for the Linear Sampling Method available, which we adapted to implement the MUSIC-type reconstruction method presented here.

Last, but not least, we like to express our gratitude to Habib Ammari for his continous support, and for many interesting discussions in the course of this project.

References

[1] H. Ammari, E. Iakovleva, D. Lesselier, and G. Perrusson, *MUSIC–type electromagnetic imaging of a collection of small three–dimensional bounded inclusions*, SIAM J. Sci. Comput. **29** (2007), no. 2, 674–709.

[2] H. Ammari and H. Kang, *Reconstruction of Small Inhomogeneities from Boundary Measurements*, Lecture Notes in Math., vol. 1846, Springer–Verlag, Berlin, 2004.

[3] ———, *Polarization and Moment Tensors with Applications to Inverse Problems and Effective Medium Theory*, Appl. Math. Sci., vol. 162, Springer–Verlag, Berlin, 2007.

[4] H. Ammari, H. Kang, E. Kim, and M. Lim, *Reconstruction of closely spaced small inclusions*, SIAM J. Numer. Anal. **42** (2005), no. 6, 2408–2428.

[5] W.L. Anderson, *Numerical integration of related Hankel transforms of orders 0 and 1 by adaptive digital filtering*, Geophysics **44** (1979), no. 7, 1287–1305.

[6] B. Borchers, *Hankel Transform Routines in MATLAB,* `http://infohost.nmt.edu/~borchers/hankel.html`, 2001.

[7] M. Brühl, M. Hanke, and M.S. Vogelius, *A direct impedance tomography algorithm for locating small inhomogeneities*, Numer. Math. **93** (2003), 635–654.

[8] M. Cheney, *The linear sampling method and the MUSIC algorithm*, Inverse Problems **17** (2001), no. 4, 591–595.

[9] D. Colton and R. Kress, *Inverse Acoustic and Electromagnetic Scattering Theory*, 2nd ed., Appl. Math. Sci., vol. 93, Springer–Verlag, Berlin, 1998.

[10] P.–M. Cutzach and C. Hazard, *Existence, uniqueness and analyticity properties for electromagnetic scattering in a two–layered medium*, Math. Methods Appl. Sci. **21** (1998), no. 5, 433–461.

[11] G. Dassios and R. Kleinman, *Low Frequency Scattering*, Oxford Math. Monogr., Oxford University Press, New York, 2000.

[12] F. Delbary, K. Erhard, R. Kress, R. Potthast, and J. Schulz, *Inverse electromagnetic scattering in a two–layered medium with an application to mine detection*, Inverse Problems **24** (2008), no. 1, 015002 (18 pp.)

[13] A.J. Devaney, *Super–resolution processing of multi–static data using time reversal and MUSIC*, Preprint, Department of Electrical Engineering, Northeastern University, Boston, MA (1999).

[14] A. Friedman and M.S. Vogelius, *Identification of small inhomogeneities of extreme conductivity by boundary measurements: a theorem on continuous dependence*, Arch. Rational Mech. Anal. **105** (1989), no. 4, 299–326.

[15] B. Gebauer, M. Hanke, A. Kirsch, W. Muniz, and C. Schneider, *A sampling method for detecting buried objects using electromagnetic scattering*, Inverse Problems **21** (2005), no. 6, 2035–2050.

[16] R. Griesmaier, *Detection of Small Buried Objects: Asymptotic Factorization and MUSIC*, Dissertation, Johannes Gutenberg–Universität, Mainz, 2008, `http://nbn-resolving.de/urn/resolver.pl?urn=urn:nbn:de:hebis:77-16663`.

[17] ———, *An asymptotic factorization method for inverse electromagnetic scattering in layered media*, SIAM J. Appl. Math. **68** (2008), no. 5, 1378–1403.

[18] *HuMin/MD — Metal detectors for humanitarian demining — Development potentials in data analysis methodology and measurement,* Project Network, `http://www.humin-md.de/`.

[19] E. Iakovleva, S. Gdoura, D. Lesselier, and G. Perrusson, *Multistatic response matrix of a 3–D inclusion in half space and MUSIC imaging*, IEEE Trans. Antennas Propagat. **55** (2007), no. 9, 2598–2609.

[20] E. Iakovleva and D. Lesselier, *Multistatic response matrix of spherical scatterers and the back–propagation of singular fields*, IEEE Trans. Antennas Propagat. **56** (2008), no. 3, 825–833.

[21] J. Igel and H. Preetz, *Elektromagnetische Bodenparameter und ihre Abhängigkeit von den Bodeneigenschaften. — Zwischenbericht Projektverbund Humanitäres Minenräumen*, Technical Report, Leibniz Institute of Applied Geosciences, Hannover (2005).

[22] A. Kirsch, *The MUSIC algorithm and the factorization method in inverse scattering theory for inhomogeneous media*, Inverse Problems **18** (2002), no. 4, 1025–1040.

[23] P. Monk, *Finite Element Methods for Maxwell's Equations*, Numer. Math. Sci. Comput., Oxford University Press, New York, 2003.

[24] C. Schneider, *Visualisierung vergrabener Objekte: Ein Sampling-Verfahren für die Maxwell-Gleichungen*, Dissertation, Johannes Gutenberg–Universität, Mainz, in preparation.

Department of Mathematical Sciences, University of Delaware, Newark, Delaware 19716, U.S.A.
E-mail address: `griesmai@math.udel.edu`

Institut für Mathematik, Johannes Gutenberg-Universität, 55099 Mainz, Germany
E-mail address: `hanke@math.uni-mainz.de`